Check for updates

View Article Online
View Journal

Chemical Science

Accepted Manuscript

This article can be cited before page numbers have been issued, to do this please use: X. Ai, C. Liu, Z. Li, Y. Zhang, S. Liu, H. Xiong and J. Li, *Chem. Sci.*, 2026, DOI: 10.1039/D6SC00447D.

Chemical Science
Volume 9
Number 1
7 January 2018
Pages 1-268
rsc.li/chemical-science
ISSN 2041-6539
ROYAL SOCIETY OF CHEMISTRY
EDGE ARTICLE
Xinjing Tang *et al.*
Caged circular siRNAs for photomodulation of gene expression in cells and mice

This is an Accepted Manuscript, which has been through the Royal Society of Chemistry peer review process and has been accepted for publication.

Accepted Manuscripts are published online shortly after acceptance, before technical editing, formatting and proof reading. Using this free service, authors can make their results available to the community, in citable form, before we publish the edited article. We will replace this Accepted Manuscript with the edited and formatted Advance Article as soon as it is available.

You can find more information about Accepted Manuscripts in the Information for Authors.

Please note that technical editing may introduce minor changes to the text and/or graphics, which may alter content. The journal's standard Terms & Conditions and the Ethical guidelines still apply. In no event shall the Royal Society of Chemistry be held responsible for any errors or omissions in this Accepted Manuscript or any consequences arising from the use of any information it contains.

ROYAL SOCIETY OF CHEMISTRY

rsc.li/chemical-science

View Article Online
DOI: 10.1039/D6SC00447D

Lattice strained Na-$ZnFe_2O_4$ catalyst boosting CO_2 hydrogenation to long-chain olefins.

Received 00th January 20xx,
Accepted 00th January 20xx

DOI: 10.1039/x0xx00000x

Xinyan Ai[†a], Chengchao Liu[†a,*], Zhe Li[†a], Yuhua Zhang[a], Sixu Liu[b,c], Haifeng Xiong[b,c,*], and Jinlin Li[a,*]

Thermo-catalytic hydrogenation of CO_2 to fuels and chemicals is an effective way for the utilization of CO_2, yet it faces significant challenges due to the low CO_2 conversion and product selectivity. Here, we report a lattice-strained FeZnNa catalyst synthesized via mechanochemical method (FeZnNa-G), showing the high selectivity of C_{4+} long-chain olefins ($C_{4+}^{=}$) of 64.9% and C_{2+}= of 77.5% at a high CO_2 conversion of 47.7%. We found that the lattice-contracted FeZnNa-G catalyst forms Na-enriched ZnO nano-islands on the surface after activation and a Na-ZnO/Fe_5C_2 structure with the presence of 97% Fe_5C_2, facilitating the formation of $HCOO^*$ intermediate and enhancing CO_2 activation. A high $C_{4+}^{=}$ space-time yield (STY) of 474.9 $mg \cdot g_{cat}^{-1} \cdot h^{-1}$ and an extremely low CO selectivity of ~9.1% exhibited the dual-high performance significantly surpassing the previous reports. This use of lattice strained catalyst offers a new strategy for the efficient conversion of CO_2 into high-value olefins, and paves the way for the potential industry application in future.

Introduction

With the continuous growth of the global economy and energy demand, the massive consumption of carbon-based energy has led to a sharp increase in CO_2 emissions, causing environmental issues such as global warming and ocean acidification [1–3]. Driven by the pursuit of clean energy and carbon neutrality, the development of efficient and sustainable CO_2 conversion technologies has become a research focus in the field of chemical engineering research. Long-chain olefins serve as fundamental chemical feedstocks, with applications spanning critical sectors such as plastics, rubber, fine chemicals and fuel additives [4–6]. Typically, C_{4+} olefins are obtained through fossil-based pathways such as short-chain olefin polymerization, alkane dehydrogenation, and the recovery of petrochemical byproducts. In contrast, directly catalyzing the hydrogenation of CO_2 into high-value long-chain olefins not only reduces atmospheric CO_2 emissions but also reduces over-dependence on fossil fuels and provides an important pathway for carbon recycling[7–12].

To date, oxide-zeolite bifunctional catalysts and Fe-based catalysts have demonstrated excellent performance in the hydrogenation of CO_2 to hydrocarbons. Bifunctional catalyst systems exhibit high selectivity for olefins and aromatics but are limited by low CO_2 conversion and high CO selectivity (> 40%)[13–16]. In contrast, Fe-based catalysts via the CO_2-Fischer-Tropsch synthesis (CO_2-FTS) pathway, leverage the formation of iron oxides and iron carbides to activate the RWGS and FTS reactions, showing advantages in the production of long-chain hydrocarbons[17–21]. However, the inherent stability of CO_2 molecules makes activation challenging, and the thermodynamic equilibrium of the RWGS reaction limits the CO_2 conversion efficiency. Moreover, the complex and variable phases of Fe catalysts during the reaction make the CO_2-FTS pathway constrained, presenting significant challenges in the efficient conversion of CO_2 into long-chain olefins.

Fe_5C_2 as a critical active species commonly encountered in Fischer-Tropsch synthesis (FTS), exhibits excellent C-C coupling ability, facilitating the production of long-chain hydrocarbons [22–25]. Studies have shown that introducing transition metals (e.g. Mn, Zn and Cu)[26–30] and alkali metals (e.g. Na, K)[31–35] as promoters into Fe-based catalysts can significantly enhance the formation of Fe_5C_2 and improve catalytic performance. Notably, Zn and Na receiving significant attention due to their pronounced effects. For example, Yang et al.[36] reported that the formation of Fe_3O_4 and Fe_5C_2 as active phases led to the high reaction activity and stability in CO_2-FTS for selective synthesis of olefins. Zn was reported to act as a structural promoter to improve the dispersion of Fe species, while Na serves as an electronic promoter to enhancing CO activation, resulting in excellent olefin selectivity during CO hydrogenation [37].

---

[a] Key Laboratory of Catalysis and Energy Materials Chemistry of Ministry of Education & Hubei Key Laboratory of Catalysis and Materials Science, South-Central Minzu University, Wuhan 430074, China.
[b] The State Key Laboratory of Physical Chemistry of Solid Surfaces, iChEM (Collaborative Innovation Center of Chemistry for Energy Materials), Department of Chemistry, College of Chemistry & Chemical Engineering, Xiamen University, Xiamen, 361005, China.
[c] Innovation Laboratory for Sciences and Technologies of Energy Materials of Fujian Province (IKKEM), 4221 Xiangan South Road, Xiamen, 361102, P. R. China.

† These authors contributed equally to this work.

Supplementary Information available: [details of any supplementary information available should be included here].

View Article Online
DOI: 10.1039/D6SC00447D

However, Zhang et al.[38] suggested that ZnO activated CO_2 to produce CO and Na primarily suppresses the secondary hydrogenation of olefins over a Na- and Zn-promoted iron catalyst. On a bimetallic Fe_5C_2-ZnO catalyst [39], the *in-situ* formation of ZnO and the highly dispersed FeO_x species on the catalyst surface enables the RWGS reaction to proceed, with the presence of FeC_x species promoting C-C coupling and alkene synthesis towards CO_2 hydrogenation. Despite these studies on the FeZnNa system reported, the effects of structural evolution of Zn and Na promoters during reduction, activation, and reaction processes on the phase and performance of Fe catalysts remain unclear. Regulating the catalyst structure and elucidating the mechanisms of promoters and Fe species in Fe-based catalysts are key to achieving efficient catalytic hydrogenation of CO_2 to long-chain olefins.

In this study, we systematically compared spinel FeZnNa catalysts prepared by wet impregnation, co-precipitation, and mechanochemical methods. Through characterization techniques such as high-resolution transmission electron microscopy, X-ray absorption spectroscopy, Mössbauer spectroscopy and density functional theory calculations, we found the structural evolution of Na-$ZnFe_2O_4$ catalysts in the CO_2 hydrogenation, which is favorable to long-chain olefins. The FeZnNa-G catalyst synthesized via the mechanochemical method exhibited the significant lattice contraction strain, which facilitated reduction and carburization, achieving a Na-ZnO enriched Fe_5C_2 catalyst with 96.7% Fe_5C_2 content.

Results and Discussion

Catalytic CO_2 hydrogenation performance

FeZnNa-I, FeZnNa-C, and FeZnNa-G catalysts were prepared using impregnation, co-precipitation, and mechanochemical methods, respectively, with elemental compositions listed in Table S1. The catalytic performance of the catalysts for CO_2 hydrogenation was first evaluated at different reaction temperatures (Tables S2 and S3). As shown in the results, the FeZnNa-G catalyst exhibits higher catalytic activity than the other catalysts at the same reaction temperature. From the variation in product selectivity, a relatively high CO selectivity is observed at lower temperatures. With increasing temperature, the CO selectivity gradually decreases, while the selectivity toward hydrocarbons correspondingly increases, indicating that the reaction over this series of catalysts mainly follows a modified RWGS-FTS reaction pathway. Under lower space velocity conditions, the CO_2 conversion of the catalysts can reach above 40%, whereas the CO selectivity decreases slightly. This is attributed to the longer residence time of reactant molecules on the catalyst surface, which facilitates the continuous occurrence of the subsequent FTS reaction. However, due to the thermodynamic equilibrium limitation of the CO_2 hydrogenation reaction, increasing the reaction space velocity is more favorable for distinguishing the differences in catalytic active sites. Therefore, the catalytic performance for CO_2 hydrogenation was systematically evaluated under reaction conditions of 340 °C, H_2:CO_2:N_2= 67.5:22.5:10, 2 MPa, and a GHSV of 12000 mL·g^{-1}·h^{-1}. As shown in Fig. 1a and Table S3, the CO_2 conversion over the FeZnNa-I and FeZnNa-C catalysts was 38.6% and 35.4% respectively, with selectivities toward $C_{2+}^{=}$ olefins of 66.3% and 54.1%. Among these products, the selectivities to long-chain $C_{4+}^{=}$ olefins were 43.8% and 34.3%, respectively, indicating that the impregnation method is more favorable for the formation of long-chain olefins than coprecipitation. Notably, the mechanochemically obtained FeZnNa-G catalyst exhibited a markedly enhanced CO_2 conversion of 47.7%. The selectivity to $C_{2+}^{=}$ products increased to 77.5%, within which long-chain $C_{4+}^{=}$ accounted for 83.7%, corresponding to a $C_{4+}^{=}$ selectivity of 64.9% (Fig. 1a-b). Meanwhile, the formation of undesired CO and CH_4 was effectively suppressed to 9.1% and 7.3%, respectively. No obvious deactivation was observed for any of the catalysts during 108 h of continuous stability testing (Fig. 1c and Fig. S1). Compared with previously reported catalysts under comparable reaction conditions (Fig. 1c and Table S3), the mechanochemically synthesized FeZnNa-G catalyst achieved a long-chain $C_{4+}^{=}$ space-time yield (STY) of 474.9 mg·g$_{cat}^{-1}$·h^{-1}, demonstrating a significant advantage. This FeZnNa-G catalyst not only achieved 'dual high' performance in CO_2 conversion and $C_{4+}^{=}$ product selectivity but also substantially suppressed the formation of low-value by-products such as CO and CH_4.

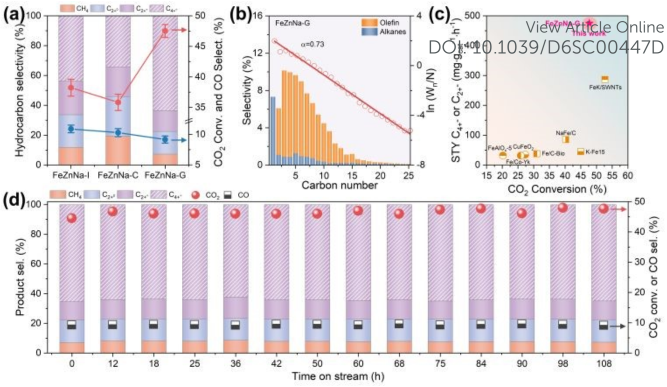

Fig. 1 Catalytic properties. (a) catalytic performance on Fe based catalysts, (b) the product distribution and Anderson-Schulz-Flory (ASF) plots of FeZnNa-G catalysts. (c) the relationship of STY with CO_2 conversion over various catalysts (ref. in Supporting Information). (d) The stability of FeZnNa-G catalysts CO_2 hydrogenation reaction at 340 °C, 2.0 MPa, 12000 mL·g^{-1}·h^{-1}, H_2/CO_2=3.

Structural characteristics and phase evolution of catalysts

X-ray diffraction (XRD) (Fig. S2) shows that the main phase of the catalysts is the spinel-type $ZnFe_2O_4$. The magnified patterns reveal that for the FeZnNa-G catalyst, compared to the other two FeZnNa catalysts, its characteristic diffraction peaks shifted towards higher angles, indicating the lattice contraction. Table S6 shows the physical properties of the catalyst, where the FeZnNa-G catalyst has a smaller particle size. The morphology of the FeZnNa catalysts was characterized by TEM. As shown in Fig. S3-S5, the catalysts were granular and EDS analysis showed that the elements were uniformly dispersed. High-resolution transmission electron microscopy (HRTEM) images and interplanar spacing data (Fig. 2a to f) showed that the lattice

View Article Online
DOI: 10.1039/D6SC00447D

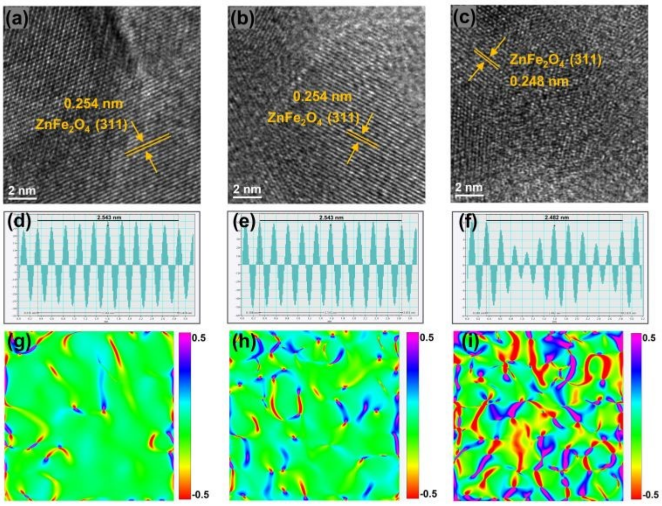

Fig. 2 Structure characterization of the FeZnNa catalysts. HRTEM images of the as-prepared (a) FeZnNa-I, (b) FeZnNa-C and (c) FeZnNa-G catalysts, (d-f) corresponding intensity profiles of a-c, (g-i), Corresponding strain maps of geometrical phase analysis (GPA) for HRTEM images.

spacing of FeZnNa-I and FeZnNa-C was 0.254 nm, while that of FeZnNa-G was 0.248 nm, corresponding to the (311) plane of $ZnFe_2O_4$. Notably, the lattice spacing in the FeZnNa-G catalyst was reduced, with distinct lattice dislocations and distortions. To better visualize the contraction state of the catalyst, strain maps were generated from the HRTEM images using geometric phase analysis (GPA, Fig. 2g-i), further confirming the lattice contraction strain in FeZnNa-G.

The phase analysis of the catalysts after the reaction (Fig. 3a-e) shows that the catalysts underwent significantly different phase transitions during the reaction process. FeZnNa-I exhibits pronounced Fe_3O_4 characteristic peaks and faint Fe_5C_2 peaks, while FeZnNa-C displays prominent Fe_3O_4 peaks and weak ZnO peaks and the significant Fe_5C_2 and ZnO peaks are observed in FeZnNa-G. The Fe_5C_2 content in catalysts after the reaction was 50.6%, 30.7%, and 96.7% for FeZnNa-I, FeZnNa-C, and FeZnNa-G, respectively (Table S7). It is generally believed that in the CO_2-FTS process over Fe catalysts, Fe_xO acts as the active center for the RWGS reaction, responsible for activating CO_2 to produce CO, while Fe_xC catalyzes the further hydrogenation of CO to hydrocarbon products[41–44]. Fe_5C_2 with rich electronic properties has been confirmed as a highly active phase for converting CO into olefins[27]. After the reaction, the FeZnNa-G catalyst with lattice contraction strain achieved a high Fe_5C_2 active phase content of 96.7%, facilitating C-C coupling and thus enhancing $C_{4+}^{=}$ olefins selectivity to 64.9% and achieving 47.7% CO_2 conversion. The STY of $C_{4+}^{=}$ long-chain olefins reached up to 474.9 $mg\cdot g_{cat}^{-1}\cdot h^{-1}$, where the high content of Fe_5C_2 was key to the increased selectivity for long-chain olefins.

Surface structural evolution during reaction

The surface structural changes of the catalyst and their evolution during the reaction process were further examined. The X-ray absorption near-edge structure (XANES) results at the Fe K-edge (Fig. S6) show that the Fe chemical states in the catalysts are similar to those in Fe_2O_3. The comparison of the white-line peak intensities indicates that the oxidation state of Fe in FeZnNa-G is lower. The Fe 2p XPS results for fresh catalysts (Fig. 4a) show Fe^{3+}/Fe^{2+} ratios of FeZnNa-C=2.04 > FeZnNa-I=1.67 > FeZnNa-G=1.26, consistent with the XANES findings. Additionally, the lower Fe^{3+}/Fe^{2+} ratio on the surface of the reduced FeZnNa-G suggests that its surface contains more low-valent Fe species, which is more conducive to the occurrence of the reduction and carbonization processes. Further analysis of the surface components of the catalyst before and after the reaction was conducted. The results in Tables S8 and S9 show that the Zn/Fe and Na/Fe ratios on the catalyst surface increased significantly after the reaction, indicating that Zn and Na migrated from the bulk phase to the surface during the reaction process. Notably, FeZnNa-G exhibits the highest migration ratios for Zn and Na. In addition, the O1s spectrum in Fig. 4c shows that the peak area ratios of Odef in FeZnNa-I, FeZnNa-C, and FeZnNa-G catalysts are 37.0%, 44.8%, and 62.8%, respectively, indicating that the mechanochemical method facilitates the generation of more oxygen vacancies on the catalyst surface.

To reveal the structural changes on the surface of the catalyst, the morphology of the catalysts after the reaction was characterized (Fig. 4d-f). In the FeZnNa-G catalyst, uniformly dispersed ZnO particles form on the Fe_5C_2 surface, and EDS line-scan analysis performed across multiple regions show that the intensities of Zn and Na are highly synchronized and are mainly enriched at the edge regions of the Fe particles (Fig.S9), indicating a strong interaction between Na and ZnO. As shown in the inset of Figure 4G, after the reaction, the closely associated Na-ZnO is well enriched on the Fe_5C_2 surface, forming the Na-ZnO/Fe_5C_2 structure. In contrast, for the FeZnNa-I catalyst, although Zn and Na are closely associated, ZnO is only partially enriched on the surface of the Fe species (Fig. S7). For the FeZnNa-C catalyst, ZnO is neither enriched on the Fe surface nor closely associated with Na, highlighting the significant differences in the structural evolution among the catalysts (Fig. S8).

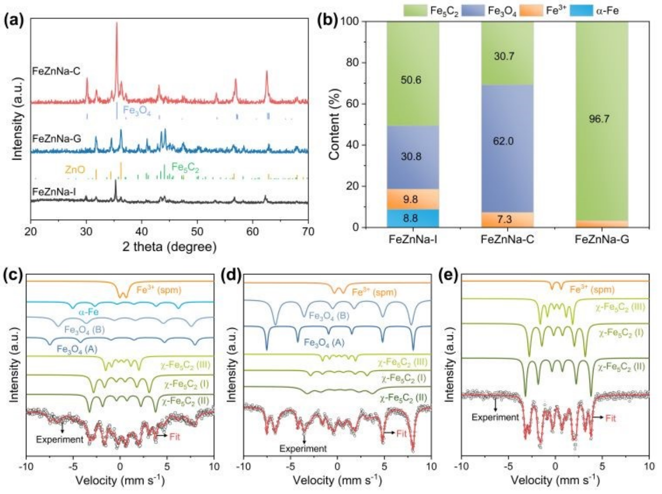

Fig. 3 Composition and microstructure of catalysts after CO_2 hydrogenation reaction. (a) XRD patterns of the spent catalysts, (b) Fe species content. MÖssbauer spectra of the (c) FeZnNa-I, (d) FeZnNa-C, (e) FeZnNa-G catalysts after reaction.

View Article Online
DOI: 10.1039/D5SC09447B

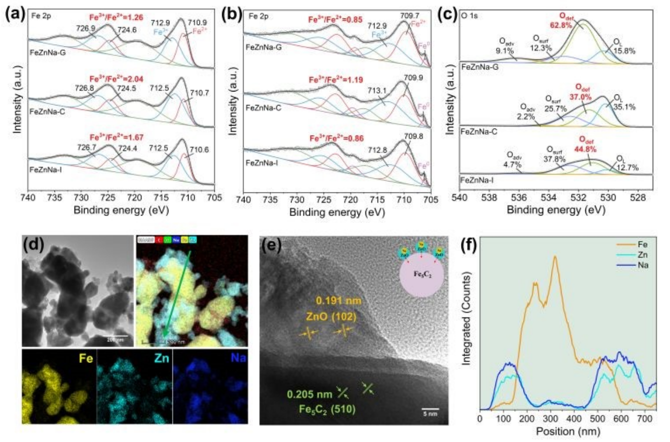

Fig. 4 Fe 2p XPS spectra of the (a) as-prepared catalysts and (b) reduced catalysts. (d) TEM images and corresponding elemental mapping, (e) HRTEM images and (f) line scanning profile of the arrow in (d).

Reduction behavior and adsorption properties

The reduction behavior of the catalyst has a significant impact on the formation of the active phase. H_2 temperature-programmed reduction (H_2-TPR) results (Fig. S10) show that compared to FeZnNa-C, the FeZnNa-I catalyst exhibits a lower reduction temperature, while the FeZnNa-G catalyst demonstrates stronger reduction intensity, indicating that under the reduction temperature of 400 °C, the catalyst exhibits a higher reduction degree, providing a larger amount of reducible iron oxides and thus supplying more metallic Fe precursors for the subsequent carburization process. After reduction at 400 °C with H_2 for 2 h (Fig. S11), the phase of FeZnNa-I and FeZnNa-G shifted primarily from $ZnFe_2O_4$ to ZnO, FeO, and Fe, with FeZnNa-G showing a higher ZnO peak intensity, indicating that Zn is more easily segregated to form ZnO upon reduction in FeZnNa-G. Additionally, its relatively higher metal Fe characteristic peak further supported that the reduction degree was higher. In contrast, the phase of FeZnNa-C after reduction was mainly ZnO, Fe_3O_4, and Fe, retaining a significant amount of Fe_3O_4, suggesting that the reduction of Fe species in this catalyst is inhibited.

Clearly, the FeZnNa-G catalyst synthesized via the mechanochemical method facilitates the migration of Zn and Na to the catalyst surface forms Na-ZnO nano-islands during reduction and activation. As an electron-donating promoters, the surface enrichment of Zn and Na significantly influences the adsorption properties of the catalyst. To further investigate this observation, CO_2 temperature-programmed desorption (CO_2-TPD) tests were conducted on the post-reaction catalysts. As shown in Fig. S12a, FeZnNa-G exhibits the significantly stronger desorption peaks, indicating that the enrichment of Na-ZnO on the Fe_5C_2 surface greatly enhances CO_2 adsorption and activation. Moreover, the ability of the catalyst to adsorb CO is also critical in CO_2 hydrogenation. Strong CO adsorption facilitates the second step of the FTS reaction, promoting the further hydrogenation to long-chain hydrocarbons while reducing the formation of CO as a by-product[45]. According to the CO temperature-programmed desorption (CO-TPD) results (Fig. S12b), FeZnNa-G presents the strong desorption peaks, indicating a higher CO adsorption capacity. This ability to adsorb more CO benefits the conversion of CO intermediates during the reaction, thereby improving the $C_{4+}^{=}$ selectivity while simultaneously reducing the selectivity for CO.

Intrinsic role of lattice strain

From the above characterization results, it can be seen that the FeZnNa-G catalyst prepared by mechanochemical method shows a higher content of Fe_5C_2. During the reaction, Zn and Na are more likely to migrate to the surface to form a stable Na-ZnO complex, and it has a higher degree of reduction and adsorption capacity for reaction molecules, significantly promoting the efficient generation of long-chain olefins from CO_2 hydrogenation. More importantly, compared with other FeZnNa catalysts, the FeZnNa-G catalyst prepared by mechanochemical method has a certain degree of lattice contraction. The lattice strain values were calculated using the Williamson-Hall method[40]. Here, the analysis is mainly used to provide a comparative evaluation of lattice strain among catalysts prepared by different methods. As shown in Fig. 5a, the FeZnNa-G catalyst exhibited a lattice strain (ε) of 0.774, significantly higher than that of FeZnNa-I (ε=0.390) and FeZnNa-C (ε=0.395), confirming the significant lattice strain in the FeZnNa-G catalyst. Furthermore, the Fe K-edge extended X-ray absorption fine structure (EXAFS) results (Fig. 5b and Table S10) reveal that the Fe-Zn bond distance in FeZnNa-G (2.94Å) is shorter than in FeZnNa-I (2.96Å) and FeZnNa-C (2.97Å). This indicates that the lattice contraction strain induced by the mechanochemical method reduces the distance between Fe and Zn atoms in the catalyst. The closer Fe-Zn contact distance is expected to enhance the promoting effect of Zn on metallic Fe.

To clarify the fundamental cause of the strain generated by the catalyst, the mechanochemical method was employed to prepare FeZnNa-G catalysts with varying Na content, milling time, and milling method. The XRD patterns and strain data for catalysts (Figs. S13 and S14) show that in the absence of Na, the

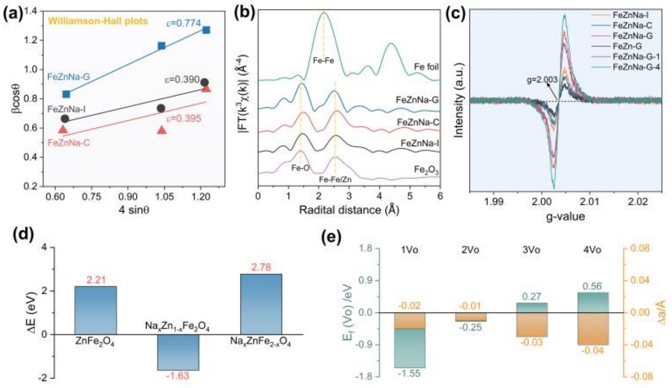

Fig. 5 Structure characterization and DFT theoretical calculations. (a) Williamson-Hall plots of the Fe-based catalysts. (b) Fourier transformed EXAFS data for these FeZnNa catalysts. (c) Electron Paramagnetic Resonance diagram of the FeZn catalysts. (d) DFT calculation of the doping reaction energy (ΔE) of Na. (e) The formation energy (E_f) of oxygen vacancy (V_O) in Na-doping $ZnFe_2O_4$ and the lattice constant variation referring to the pristine $ZnFe_2O_4$.

View Article Online
DOI: 10.1039/D6SC00447D

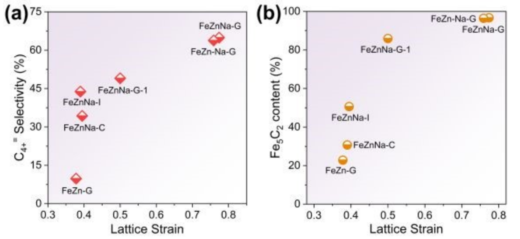

Fig. 6 Correlation diagram of the lattice strain with (a) Fe_5C_2 content and (b) $C_{4+}^{=}$ selectivity.

strain value of the FeZn-G catalyst is 0.378, which is similar to that of the FeZnNa-I and FeZnNa-C catalysts prepared by impregnation and precipitation methods. However, when Na is introduced, the catalyst undergoes strain, and the strain increases with the increase of Na content. Meanwhile, by introducing Na later and using the mechanochemical method, the FeZn-Na-G catalyst was prepared, and the strain value obtained is similar to that of the FeZnNa-G catalyst, indicating that the formation of strain is significantly related to Na.

Density functional theory calculations were performed to understand the lattice contraction induced by mechanical processing. The doping of sodium ion into the lattice of $ZnFe_2O_4$ spinel was considered by replacing the Zn/Fe atoms (Fig. 5d). The doping reaction energy (ΔE) of Na-to-Zn is negative (-1.63 eV) indicating the favorable replacement of the tetrahedral coordinated Zn by Na ion. However, it is positive (2.78 eV) for Na-to-Fe because of the higher binding energy (11.01 eV) of Fe with octahedral coordination than that (7.20 eV) of the Zn. Moreover, the negative formation energy (E_f = -1.55 and -0.25 eV) of the 1st and 2nd oxygen vacancy ($1V_O$ and $2V_O$) in Na-doped $ZnFe_2O_4$ spinel (Fig. 5e) indicates that the favorable removal of oxygen by H_2 reduction leading to the slight contraction of lattice constant (-0.02 ~ -0.01 Å). Oxygen vacancies characterization further confirmed that the mechanical-chemical method facilitated the incorporation of sodium into the $ZnFe_2O_4$ lattice (Fig. 5f), thereby inducing lattice contraction and generating oxygen vacancies. This enhanced the reduction degree of the catalyst, making the Fe oxide more prone to carbonization during the reaction to form Fe_5C_2, and facilitating the migration of Zn and Na to the surface during the reaction, ultimately forming a tightly bound Na-ZnO/Fe_5C_2 structure.

To clarify the impact of lattice contraction strain on iron carbide formation and $C_{4+}^{=}$ selectivity, the CO_2 hydrogenation performance of FeZnNa-G catalysts with varying contraction strains was tested (Table S11), and the Fe species content after reaction was characterized by Mössbauer spectroscopy (Fig. S15, Table S7). The results show a positive correlation between Fe_5C_2 content and $C_{4+}^{=}$ selectivity with the contraction strain (Fig. 6a-b). When the strain (ε) reaches approximately 0.7, the Fe_5C_2 content stabilizes at above 90%, and the $C_{4+}^{=}$ selectivity remains at around 64%. These results indicate that the lattice contraction strain induced by the mechanical-chemical method facilitates the formation of Fe_5C_2. This is attributed to the fact that oxygen vacancies generated by lattice contraction enhance the degree of reduction, providing more metallic Fe precursors for the subsequent carburization process. thereby promoting the carburization of the catalyst during activation and increasing the Fe_5C_2 content. Given the superior chain growth capability of Fe_5C_2 as a vital active phase for long-chain olefin production, the lattice contraction significantly tailors the catalytic performance by modulating the carburization efficiency.

Reaction Mechanisms

To elucidate the reaction mechanism, in situ DRIFTS experiment was employed to investigate the reaction pathways for the catalysts during the reaction (Fig. 7a), the absorption bands at 2177 cm^{-1} and 2110 cm^{-1}, and at 2062 cm^{-1}, are attributed to gaseous CO and linearly adsorbed CO, respectively[46]. Initially, there were virtually no adsorption peaks, but with increasing reaction time, the peak intensity continuously strengthened, indicating that the RWGS reaction generating CO intermediate occurred first on the catalysts. The bands at 1341 cm^{-1}, 1512 cm^{-1}, and 1694 cm^{-1}, and between 1610-1647 cm^{-1}, are assigned to carbonate (CO_3^*) and bicarbonate (HCO_3^*) intermediates, typically considering as the products of primary CO_2 adsorption. The bands between 1523-1540 cm^{-1} correspond to carboxylate ($COOH^*$), an important intermediate in the CO_2 hydrogenation process[47]. Notably, for the FeZnNa-G catalyst, a distinct adsorption band for formate ($HCOO^*$) appeared at 1395 cm^{-1} [48–50]. Furthermore, the carboxylate ($COOH^*$) peak at 1523 cm^{-1} was significantly enhanced initially but weakened over time as it was progressively converted into formate ($HCOO^*$), suggesting that $COOH^*$ undergoes hydrogenation to form $HCOO^*$ during the reaction. Previous study[51] has reported that the RWGS reaction of CO_2 on ZnO mainly proceeds through the $HCOO^*$ intermediate. intermediate, reduces the apparent activation energy, and enhances the catalytic activity. Clearly, the surface-

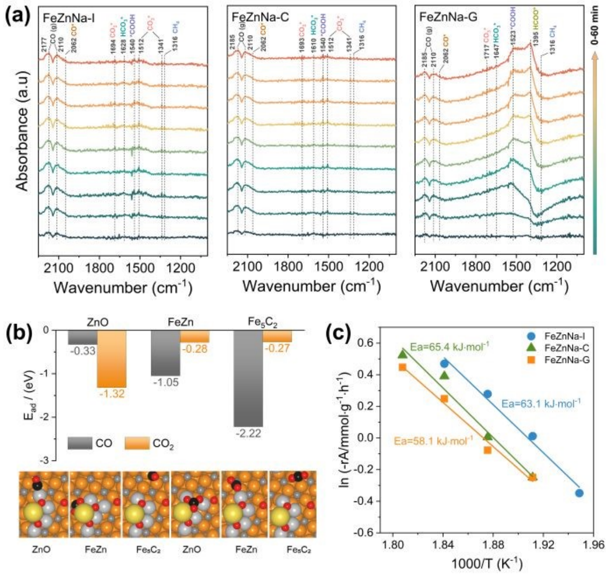

Fig. 7 Reaction mechanism studies and Schematic diagram. (a) In situ DRIFTS spectra during CO_2 hydrogenation of FeZnNa-I, FeZnNa-C and FeZnNa-G catalysts. (b) The CO/CO_2 adsorption energy (E_{ad}) and structures at different positions (ZnO, FeZn, Fe_5C_2) on the χ-Fe_5C_2 (510) surface, (c) Activation energies for CO_2 conversion on catalysts.

View Article Online
DOI: 10.1039/D6SC00447D

enriched Na-ZnO plays a vital role in CO_2 activation during the reaction. In the FeZnNa-G catalyst, as the reaction progressed,Na-enriched ZnO particles migrated to the Fe_5C_2 surface forming the Na-ZnO/Fe_5C_2 structure. The surface-enriched Na-ZnO and Fe_5C_2 synergistically promoted the formation of $HCOO^*$ intermediates, providing a new pathway for the continuous activation of CO_2. The activated CO then adsorbed on Fe_5C_2 and underwent C-C coupling to produce long-chain olefins. DFT calculations further demonstrated the favorable adsorption of CO_2 and CO on Na-ZnO-promoted Fe_5C_2 surfaces (Fig. 7b). CO_2 prefers to adsorb on the ZnO site (E_{ad} = -1.32 eV), while CO favours to bind to the Fe_5C_2 surface (E_{ad} = -2.22 eV). The highly dispersed Na-ZnO species on the surfaces of the FeZnNa-G catalyst favours to the sequential coupling between the CO_2 and CO activations. In the CO_2 hydrogenation reaction, CO_2 activation is critical for sustaining the reaction, as more effective CO_2 activation facilitates the subsequent reactions and increases hydrocarbon product selectivity. Kinetic analysis of the catalysts (Fig. 7c) revealed that the apparent activation energy of the FeZnNa-G catalyst synthesized by the mechanochemical method was 58.1 $kJ \cdot mol^{-1}$, lower than that of FeZnNa-I (63.1 $kJ \cdot mol^{-1}$) and FeZnNa-C (65.4 $kJ \cdot mol^{-1}$). This finding further confirms that the synergy between surface-enriched Na-ZnO and Fe_5C_2 in the FeZnNa-G catalyst promotes the formation of the $HCOO^*$

Fig. 8 illustrates the relationship between catalyst performance and structural changes. The FeZnNa-G catalyst synthesized via the mechanochemical method undergoes lattice contraction induced by the doping Na under mechanicalforce, forming oxygen vacancies that enhance the degree of reduction and promote carburization. During activation, Zn and Na readily migrate to the surface, forming Na-ZnO complexes. The synergy between Na-ZnO and the high content Fe_5C_2 facilitates the formation of $HCOO^*$ intermediate, providing a new pathway for sustained CO_2 activation. The abundant Fe_5C_2 further efficiently promotes C-C coupling, enhancing the selectivity for $C_{4+}^{=}$ long-chain olefins.

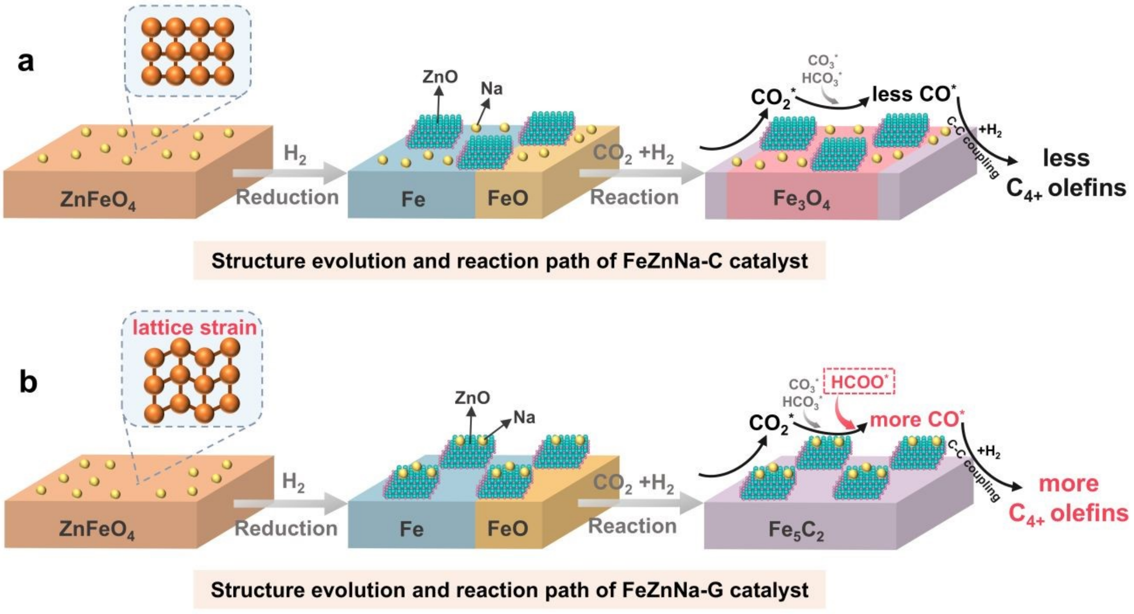

Fig. 8 Schematic diagram of the evolution and reaction path of the catalysts.

Conclusions

To overcomes the "seesaw" between activity and selectivity in CO_2 hydrogenation to long-chain olefins (C_{4+}=) over Fe-based catalysts, we synthesized a lattice-strained FeZnNa catalyst via mechanochemical approach (FeZnNa-G). Compared to the conventional FeZnNa catalysts prepared by wet impregnation and co-precipitation, the FeZnNa-G catalyst, synthesized under mechanical force, incorporates Na into the $ZnFe_2O_4$ spinel lattice, inducing lattice contraction and generating oxygen vacancies. These structural changes promote the reduction and carburization of the catalyst, leading to the extremely high content of Fe_5C_2 (96.7%) after the reaction. During the reaction, Zn and Na migrated to the surface forming a closely bound Na-ZnO structure. The Na-ZnO/Fe_5C_2 catalyst generates formate ($HCOO^*$) intermediate, providing a new pathway for continuous CO_2 activation and offering the active carbon species for the efficient C-C coupling on Fe_5C_2, thereby enhancing the production of long-chain olefins. The FeZnNa-G catalyst achieved CO_2 conversion of 47.7% and a $C_{4+=}$ long-chain olefins selectivity of 64.9%, with small amount of by-product CO of only 9.1%. The STY for $C_{4+=}$ products reached 474.9 $mg \cdot g_{cat}^{-1} \cdot h^{-1}$, demonstrating the significant advantages in converting CO_2 to long-chain olefins. The lattice-strained catalyst prepared by mechanochemistry provides the new insights and approaches for designing efficient heterogeneous catalysts.

View Article Online
DOI: 10.1039/D6SC00447D

Author contributions

Xinyan Ai conducted all experiments and characterized the catalysts. Xinyan Ai, Chengchao Liu designed the experiments. Xinyan Ai, Chengchao Liu, Zhe Li, Haifeng Xiong wrote the manuscript. Chengchao Liu, Jinlin Li were responsible for funding application and supervised the project. Zhe Li, Yuhua Zhang, Sixu Liu contributed to the analysis and interpretation of the data.

Conflicts of interest

There are no conflicts to declare.

Data availability

The authors confirm that the data supporting the findings of this study are available within the article and its supplementary information.

Acknowledgements

We acknowledge the Center for Advanced Mössbauer Spectroscopy, Dalian Institute of Chemical Physics, CAS for providing the Mössbauer measurement and analysis. We also acknowledge the Xinyue Liu from MeLab Scientific Research Platform (www.micetech.cn) for the help in the TEM and X-ray absorption spectrum characterization. This work was supported by the National Key Research and Development Program of China (2022YFB4101201), the National Natural Science Foundation of China (21902187, U22A20394), the Key Research and Development Program of Hubei Province (2022BCA084), and the Fund for Academic Innovation Teams of South-Central Minzu University (PTZ24011).

Notes and references

1 R. A. Begum, K. Sohag, S. M. S. Abdullah and M. Jaafar, *Renew. Sustain. Energy Rev.*, 2015, **41**, 594–601.

2 G. A. Olah, G. K. S. Prakash and A. Goeppert, *J. Am. Chem. Soc.*, 2011, **133**, 12881–12898.

3 G. A. Meehl, W. M. Washington, W. D. Collins, J. M. Arblaster, A. Hu, L. E. Buja, W. G. Strand and H. Teng, *Science*, 2005, **307**, 1769–1772.

4 P. Gao, S. Li, X. Bu, S. Dang, Z. Liu, H. Wang, L. Zhong, M. Qiu, C. Yang, J. Cai, W. Wei and Y. Sun, *Nature Chem*, 2017, **9**, 1019–1024.

5 M. Wang, P. Wang, G. Zhang, Z. Cheng, M. Zhang, Y. Liu, R. Li, J. Zhu, J. Wang, K. Bian, Y. Liu, F. Ding, T. P. Senftle, X. Nie, Q. Fu, C. Song and X. Guo, *Sci. Adv.*, 2023, **9**, eadg0167.

6 M. Cui, Q. Qian, J. Zhang, Y. Wang, B. B. Asare Bediako, H. Liu and B. Han, *Chem*, 2021, **7**, 726–737.

7 M. Aresta, A. Dibenedetto and A. Angelini, *Chem. Rev.*, 2014, **114**, 1709–1742.

8 M. He, Y. Sun and B. Han, *Angew. Chem. Int. Ed.*, 2013, **52**, 9620–9633.

9 O. S. Bushuyev, P. De Luna, C. T. Dinh, L. Tao, G. Saur, J. Van De Lagemaat, S. O. Kelley and E. H. Sargent, *Joule*, 2018, **2**, 825–832.

10 M. D. Porosoff, B. Yan and J. G. Chen, *Energy Environ. Sci.*, 2016, **9**, 62–73.

11 R. W. Dorner, D. R. Hardy, F. W. Williams and H. D. Willauer, *Energy Environ. Sci.*, 2010, **3**, 884.

12 J. Wei, R. Yao, Y. Han, Q. Ge and J. Sun, *Chem. Soc. Rev.*, 2021, **50**, 10764–10805.

13 J. Liu, Y. Song, X. Guo, C. Song and X. Guo, *Chin. J. Catal.*, 2022, **43**, 731–754.

14 J. Zhang, M. Zhang, S. Chen, X. Wang, Z. Zhou, Y. Wu, T. Zhang, G. Yang, Y. Han and Y. Tan, *Chem. Commun.*, 2019, **55**, 973–976.

15 Y. Wang, L. Tan, M. Tan, P. Zhang, Y. Fang, Y. Yoneyama, G. Yang and N. Tsubaki, *ACS Catal.*, 2019, **9**, 895–901.

16 X. Zhang, A. Zhang, X. Jiang, J. Zhu, J. Liu, J. Li, G. Zhang, C. Song and X. Guo, *J. CO_2 Util.*, 2019, **29**, 140–145.

17 J. Zhu, P. Wang, X. Zhang, G. Zhang, R. Li, W. Li, T. P. Senftle, W. Liu, J. Wang, Y. Wang, A. Zhang, Q. Fu, C. Song and X. Guo, *Sci. Adv.*, 2022, **8**, eabm3629.

18 D. Wang, Z. Xie, M. D. Porosoff and J. G. Chen, *Chem*, 2021, **7**, 2277–2311.

19 G. Prieto, *Chemsuschem*, 2017, **10**, 1056–1070.

20 L. Wang, Y. Han, J. Wei, Q. Ge, S. Lu, Y. Mao and J. Sun, *Appl. Catal. B Environ.*, 2023, **328**, 122506.

21 J. Wei, Q. Ge, R. Yao, Z. Wen, C. Fang, L. Guo, H. Xu and J. Sun, *Nat. Commun.*, 2017, **8**, 15174.

22 L. Niu, X. Liu, X. Zhou, C. Huo, J. Xu, X. Wen, J. W. Niemantsverdriet, Y. Yang and Y. Li, *J. Catal.*, 2022, **407**, 97–103.

23 Q. Chang, C. Zhang, C. Liu, Y. Wei, A. V. Cheruvathur, A. I. Dugulan, J. W. Niemantsverdriet, X. Liu, Y. He, M. Qing, L. Zheng, Y. Yun, Y. Yang and Y. Li, *ACS Catal.*, 2018, **8**, 3304–3316.

24 E. De Smit, F. Cinquini, A. M. Beale, O. V. Safonova, W. Van Beek, P. Sautet and B. M. Weckhuysen, *J. Am. Chem. Soc.*, 2010, **132**, 14928–14941.

25 F. Lu, X. Chen, Z. Lei, L. Wen and Y. Zhang, *Appl. Catal. B*, 2021, **281**, 119521.

26 B. Liang, T. Sun, J. Ma, H. Duan, L. Li, X. Yang, Y. Zhang, X. Su, Y. Huang and T. Zhang, *Catal. Sci. Technol.*, 2019, **9**, 456–464.

27 Y. Xu, P. Zhai, Y. Deng, J. Xie, X. Liu, S. Wang and D. Ma, *Angew. Chem. Int. Ed.*, 2020, **132**, 21920–21928.

28 Y. H. Choi, Y. J. Jang, H. Park, W. Y. Kim, Y. H. Lee, S. H. Choi and J. S. Lee, *Appl. Catal. B Environ.*, 2017, **202**, 605–610.

29 M. Martinelli, C. G. Visconti, L. Lietti, P. Forzatti, C. Bassano and P. Deiana, *Catal. Today*, 2014, **228**, 77–88.

30 M. Al-Dossary, A. A. Ismail, J. L. G. Fierro, H. Bouzid and S. A. Al-Sayari, *Appl. Catal. B Environ.*, 2015, **165**, 651–660.

31 P. Tian, M. Gu, R. Qiu, Z. Yang, F. Xuan and M. Zhu, *Ind. Eng. Chem. Res.*, 2021, **60**, 8705–8713.

32 A. Ramirez, S. Ould-Chikh, L. Gevers, A. D. Chowdhury, E. Abou-Hamad, A. Aguilar-Tapia, J. Hazemann, N. Wehbe, A. J. Al Abdulghani, S. M. Kozlov, L. Cavallo and J. Gascon, *Chemcatchem*, 2019, **11**, 2879–2886.

33 J. Wei, J. Sun, Z. Wen, C. Fang, Q. Ge and H. Xu, *Catal. Sci. Technol.*, 2016, **6**, 4786–4793.

34 B. Liang, H. Duan, T. Sun, J. Ma, X. Liu, J. Xu, X. Su, Y. Huang and T. Zhang, *ACS Sustain. Chem. Eng.*, 2019, **7**, 925–932.

35 C. G. Visconti, M. Martinelli, L. Falbo, A. Infantes-Molina, L. Lietti, P. Forzatti, G. Iaquaniello, E. Palo, B. Picutti and F. Brignoli, *Appl. Catal. B Environ.*, 2017, **200**, 530–542.

36 H. Yang, Y. Dang, X. Cui, X. Bu, J. Li, S. Li, Y. Sun and P. Gao, *Appl. Catal. B*, 2023, **321**, 122050.

37 P. Zhai, C. Xu, R. Gao, X. Liu, M. Li, W. Li, X. Fu, C. Jia, J. Xie, M. Zhao, X. Wang, Y. Li, Q. Zhang, X. Wen and D. Ma, *Angew Chem Int Ed*, 2016, **55**, 9902–9907.

38 Z. Zhang, H. Yin, G. Yu, S. He, J. Kang, Z. Liu, K. Cheng, Q. Zhang and Y. Wang, *J. Catal.*, 2021, **395**, 350–361.

39 C. Zhang, C. Cao, Y. Zhang, X. Liu, J. Xu, M. Zhu, W. Tu and Y.-F. Han, *ACS Catal.*, 2021, **11**, 2121–2133.

View Article Online
DOI: 10.1039/D6SC00447D

40 M. Ghasemi Hajiabadi, M. Zamanian and D. Souri, *Ceram. Int.*, 2019, **45**, 14084–14089.
41 S. Saeidi, N. A. S. Amin and M. R. Rahimpour, *J. CO_2 Util.*, 2014, **5**, 66–81.
42 A. Fedorov, H. Lund, V. A. Kondratenko, E. V. Kondratenko and D. Linke, *Appl. Catal. B Environ.*, 2023, **328**, 122505.
43 X. Cui, P. Gao, S. Li, C. Yang, Z. Liu, H. Wang, L. Zhong and Y. Sun, *ACS Catal.*, 2019, **9**, 3866–3876.
44 M. Xu, X. Liu, C. Cao, Y. Sun, C. Zhang, Z. Yang, M. Zhu, X. Ding, Y. Liu, Z. Tong and J. Xu, *ACS Sustainable Chem. Eng.*, 2021, **9**, 13818–13830.
45 L. Guo, X. Gao, W. Gao, H. Wu, X. Wang, S. Sun, Y. Wei, Y. Kugue, X. Guo, J. Sun and N. Tsubaki, *Chem. Sci.*, 2023, **14**, 171–178.
46 X. Wang, C. Zeng, N. Gong, T. Zhang, Y. Wu, J. Zhang, F. Song, G. Yang and Y. Tan, *ACS Catal.*, 2021, **11**, 1528–1547.
47 M. Wang, G. Zhang, J. Zhu, W. Li, J. Wang, K. Bian, Y. Liu, F. Ding, C. Song and X. Guo, *Chem. Eng. J.*, 2022, **446**, 137217.
48 J. Zhu, G. Zhang, W. Li, X. Zhang, F. Ding, C. Song and X. Guo, *ACS Catal.*, 2020, **10**, 7424–7433.
49 L. Guo, X. Gao, W. Gao, H. Wu, X. Wang, S. Sun, Y. Wei, Y. Kugue, X. Guo, J. Sun and N. Tsubaki, *Chem. Sci.*, 2023, **14**, 171–178.
50 Q. Pan, J. Peng, S. Wang and S. Wang, *Catal. Sci. Technol.*, 2014, **4**, 502–509.
51 J. Tabatabaei, B. H. Sakakini and K. C. Waugh, *Catal. Letters*, 2006, **110**, 77–84.

View Article Online
DOI: 10.1039/D6SC00447D

Data Availability Statement

The authors confirm that the data supporting the findings of this study are available within the article and its supplementary information